Electrical Control of Glass-like Dynamics in Vanadium Dioxide for Data Storage and Processing

M. Samizadeh Nikoo[1*], R. Soleimanzadeh[1], A. Krammer[2], G. Migliato Marega[1,3], Y. Park[4], J. Son[4], A. Schueler[2], A. Kis[1,3], P. Moll[3], and E. Matioli[1*]

Metal-oxide-semiconductor junctions constitute the building block of today's electronics, providing a platform to achieve a variety of functionalities, from memories to computing. This technology, however, faces fundamental constraints for further miniaturization and compatibility with post von Neumann computing architectures, which has stimulated research on new materials and devices. Manipulation of structural, rather than electronic, states could provide a pathway towards ultra-scaled low-power functional devices, however, the electrical control of such states is not trivial. Here we report on electronically accessible long-lived structural states in Vanadium Dioxide that can offer a scheme for data storage and processing. We show that such states can be arbitrarily manipulated in short time scales and tracked beyond 10,000 seconds after excitation, exhibiting similar features of glasses. In two-terminal devices with channel lengths down to 50 nm, sub-nanosecond electrical excitation can take place with energy consumption down to 100 femto joules. These glass-like functional devices can outperform conventional metal-oxide-semiconductor electronics in terms of speed, energy consumption, and miniaturization, and open avenues for neuromorphic computation and multi-level memories.

Strongly-correlated materials, in which several physical interactions involving spin, charge, lattice, and orbital are simultaneously active, display notable electrical properties[1]. Among them, the first-order insulator-metal transition (IMT) in vanadium dioxide (VO_2) happening close to room temperature has attracted considerable interest[2-6]. From a physical point of view, understanding the underlying mechanism of phase switching in VO_2 is still a challenge in condensed matter physics, as several models ranging from Peierls- to Mott-Hubbard-type were not successful in explaining the broad range of phenomena occurring in the material[7]. Different types of excitations such as temperature, electric field, and doping can induce IMT, which makes the understanding of the phase switching more challenging[2,8]. From a technological point of view, the bulk conductivity and abrupt phase transition in VO_2 can potentially overcome some of the fundamental limitations in conventional metal-oxide-semiconductor electronics, such as the limited conductance imposed by Thomas–Fermi screening[9] and the thermionic subthreshold-slope limit imposed by Boltzmann–tyranny[10].

Besides the application of phase change materials in traditional electronics, the rich variety of phenomena in vanadium dioxide[11-15] can provide completely novel functionalities that enable new schemes for the future of electronics. Here we demonstrate an exotic property of Vanadium Dioxide — electrically controllable glass-like states — which can offer a platform for information processing and storage. We show that a two-terminal device exhibits a continuous spectrum of states that can be revealed by the incubation time of the IMT: the time at which the nucleation of phase transition percolates to form the first conductive filament between two terminals of the switch. The state can be imposed by a sequence of binary switching events and can be tracked hours after the excitation.

[1]Electrical Engineering Institute, École Polytechnique Fédérale de Lausanne (EPFL), Lausanne, Switzerland. [2]Institute of Physics, École Polytechnique Fédérale de Lausanne (EPFL), Lausanne, Switzerland. [3]Institute of Materials Science and Engineering, École Polytechnique Fédérale de Lausanne (EPFL), Lausanne, Switzerland. [4]Department of Materials Science and Engineering (MSE), Pohang University of Science and Technology (POSTECH), Pohang, 37673, Republic of Korea. ✉e-mail: mohammad.samizadeh@epfl.ch; elison.matioli@epfl.ch.

Electrical manipulation and probing of two-terminal Vanadium Dioxide devices

Fig. 1a shows an ultrafast time-domain experimental setup that can precisely collect temporal response of a two-terminal VO_2 switch (inset). The device was integrated with radiofrequency pads (ground-signal-ground configuration) which together with high-frequency probes enable accurate measurements with time resolutions down to ~5 ps (Ref.[16]). A square pulse generator applies repetitive 10-μs-long pulses with a fixed amplitude (set voltage V_{set} = 2.1 V) to a two-port 3-μm-long VO_2 switch. The waveform of the current passing through the device is measured at the 50-Ω port of a high-frequency oscilloscope, and the transient conductance of the device is extracted. Following an applied pulse, the VO_2 film exhibits initially an insulating behavior, and only after an incubation time t_{inc}, it undergoes IMT (Fig. 1b). The measurements indicate that the incubation time strongly depends on the history of the previous phase transitions. The very first switching curve presented in Fig. 1b shows an incubation time of ~1.4 μs. Triggering an IMT and measuring the incubation time after a 10-ms-long relaxation time (T) results in a 10-time shorter incubation time. Longer relaxation times after the first phase transition cause longer incubation times, however, the value of t_{inc} is still lower than that of the very first switching, even after T = 10,000 s.

Incubation time versus relaxation time, shown in Fig. 1c, indicates a logarithmic relation t_{inc} = (78 ns) log(T/(160 μs)). Although t_{inc} has a strong dependence on the previous switching events, the device conductance G_{ins} in the insulating-state (averaged over 20 ns < t < 120 ns) shows very small variations that become undetectable after ~1 s (Fig. 1d). The observed effect is qualitatively identical in micrometer- and nanometer-long devices. Fig. 1e shows incubation time versus the relative increase in conductivity for a 100-nm-long channel device. The values of incubation times are well distinguishable while the conductivity shows a very small variation, which completely relaxes after 1 second.

We note that the thermal relaxation of the device is quite fast (~100 ns, see Extended Data Fig. 1), and therefore, the heat accumulation does not play any role in these observations (inset of Fig. 1e). The memory effect observed in t_{inc} is reversible and is not due to any degradation in the film (Fig. 1f). The here-presented results correspond to a 100-nm-thick film VO_2 synthesized by sputtering on a high resistivity silicon substrate. The results were reproduced in devices with different metal contacts (Extended Data Figs. 2d-e), as well as in PLD-grown films on other substrates (Extended Data Fig. 3), supporting the generality of the effect. Our analysis also show a high device-to-device consistency (Extended Data Fig. 4).

In a following experiment, the devices were excited with a packet of N identical pulses (V_{set} = 2.1 V) and t_{inc} was monitored after a relaxation time T = 1 s (Fig. 2a). The total duration of the excitation including N pulses (ΔT = 1 ms) was much shorter than the relaxation time T. Different pulse packets result in different values of t_{inc}, indicating that such multi-pulse excitation can be used to manipulate the state of the device. Fig. 2b shows the summary of the observed results in which the measured values of t_{inc} for different values of N are presented for 60 consecutive acquisitions. These results indicate a fully-electrical scheme to manipulate and sense a Mott system (Fig. 2c). It is worth noting that the excited state does not depend on ΔT, and so the state can be induced in very short time scales (Extended Data Fig. 5). Incubation time in the evaluated devices also did not show any dependence on the width of excitation pulses and the state manipulation was achieved only through the number of triggering events.

Exploration of possible mechanisms

A) Electromigration

We explored the possible mechanisms of the observed effect. The first question was whether the electric current in the film induced the observed memory. This is a critical aspect because quasi-non-volatile memories induced by long high-current biases have been observed[17]. However this is not the case in our device, as the memory effect is independent from the excitation type and can also be induced purely by heat. Fig. 3a shows synchronized measurements in which IMT is achieved by a pulsed heater that is electrically isolated from the VO_2 switch. Every two seconds, a 20-μs-long pulse triggers IMT in the electrically isolated heaters, which ensures a temperature-driven IMT in the VO_2 switch at the middle of two heaters (see Extended Data Fig. 6). We electrically triggered the middle VO_2 switch with a period of one second and monitored the incubation time. The electrical excitation had a 20-ms time lag with respect to the heater signal (Fig. 3b). Therefore, in one electrical measurement, the VO_2 switch had a 20-ms relaxation time after a thermal-IMT, and in the next electrical measurement, the switch had a much longer relaxation (1 second) which is considered to be the reference measurement (without memory).

The results indicate that the thermally-driven IMT also induces a change in incubation time (Fig. 3c). This suggests the generality of the effect, and at the same time shows that the electric current in the film, which could induce excitation or movement of ions, does not play any role in the memory

effect since there was no current flowing in the device during the thermally-driven IMT.

B) Influence from Metal-VO_2 junction

VO_2 is an oxygen-rich thin-film and so its junction with the top metal pads forms a metal-oxide interface which might exhibit non-volatile switching, as observed in TiO_2 for example[18]. In addition, metal atoms could potentially diffuse in the VO_2 film, resulting in persistent changes in the device. Nevertheless, our experiments showed that the metal-VO_2 junction plays no role in the observed memory for the following reasons. First, we found that the effect is independent from the metal type: Ti/Au (Fig. 1), Pt, and Ti/Pt (Extended Data Figs. 2d-e). Second, we reproduced the memory effect in a cross structure (Fig. 3d), which enables triggering IMT only in the central portion of the VO_2 channel, without activating the metal-VO_2 interface. In this cross geometry, the vertical and horizontal directions (SEM image in Fig. 3d) were excited independently, with two synchronized galvanically isolated sources. The vertical path was periodically triggered every 10 s and the incubation time was monitored. Only for odd cycles (every 20 s), we activated the IMT in the horizontal direction, 1-s before triggering the vertical direction. We ensured that the phase transition area due to triggering the IMT in the horizontal direction did not reach the vertical pads (see Methods). The difference in the vertical incubation times in the odd (with 1-s memory) and even (reference) cycles shows that the memory originates from the VO_2 channel and not from the metal-VO_2 junction (Fig. 3e).

C) Long-lived metallic domains

Post-IMT intermediate super-cooled metallic domains[19,20] that can potentially persist considerably below the transition temperature is another possible mechanism that could lead to memory effects in VO_2. Electrical measurements have suggested that such metallic domains could persist up to a few milliseconds at temperatures below the IMT[13]. This was described by the classic metastability which generally exists in Mott systems with first-order transitions[21]. We performed measurements to understand whether long-lived metallic domains could play a role in our observations. Considering the very long time scales of our observed memory, one can use conventional microscopy techniques to monitor the lattice structures[22] or electronic properties[23] to directly reveal the possible existence of long-lived metallic domains in the film. Our Kelvin probe force microscopy (KPFM) measurements, however, did not show any signature of such domains, for scales greater than 30 nm at least (Extended Data Fig. 7).

We explored more in-depth the relation between long-lived metallic domains and our observations. The VO_2 cross experiment presented in Figs. 3d-e shows that such possible long-lived metallic domains have to be in the VO_2 channel and not at the metal-VO_2 junction. In this case, one expects to see a more pronounced change in incubation time for devices with shorter channels, as the channel length approaches to the size of the largest metallic domains. In the extreme case, where the channel size becomes shorter than the size of a metallic domain, the incubation time has to become zero. Such metallic domains are also expected to show a larger change in the conductance in shorter channel devices, considering the film as a resistive network. The results presented in Fig. 3f show that devices with smaller channel lengths down to 50 nm exhibit a higher increase in the conductance which could be due to possible long-lived metallic domains that could persist in millisecond time scales[13,24]. The memory embedded in the incubation time, however, was nearly constant for all gap lengths (Fig. 3f and Extended Data Fig. 8). To say the least, these results show that the possible long-lived metallic domains should have dimensions notably below 50 nm.

We also examined the IMT threshold voltage of the devices which is known to be more sensitive to the presence of long-lived metallic domains than the channel resistance[13]. The results presented in Extended Data Fig. 9 show that the threshold voltage and resistance follow the same trend, and totally relax after a few seconds, while the incubation time shows a logarithmic relaxation which keeps relaxing for orders of magnitude longer times. These measurements show that the incubation times are independent from threshold voltage and resistance changes. Although these results are not supportive of long-lived metallic domains as a main factor in our observation, due to the indirect nature of the performed measurements, they still do not totally rule out their possible contribution. Further studies such as those based on in-situ high-resolution ultrafast microscopy techniques can provide a more conclusive picture.

Structural glass-like features of the memory effect

We examined whether electronic states could be responsible for our observation. We evaluated the memory effect under a continuous-wave (CW) laser pumping with relatively high energy photons (2.33 eV), larger than the material band gap[25]. The measurements under laser excitation show a considerably higher conductivity with respect to those under dark, however, the memory effect is not affected (Figs. 4a and 4b). This observation does not support scenarios that explain the memory effect based on excitation of electronic states, such as orbital switching[26] or

trapped carrier in defects. In fact, logarithmic or stretched exponential relaxations are quite slow processes for electronic states, nevertheless, such long relaxation times are one of the main features of glassy states with configurational transitions[27]. The IMT in VO_2 is a structural switching, and therefore, slow glass-like configurational changes driven by bond lengths, vacancies, or possible long-lived metallic domains, could be a possible explanation.

To investigate this possible scenario, we evaluated the memory effect at elevated temperatures to examine an important feature of a glass-like relaxation: the system becomes more mobile close to the transition temperature[28]. In this case, an excitation signal can more easily perturbate the system, and the system relaxes faster after removing the excitation. To examine this feature, we monitored the change in incubation times between periodic pulses with separation of 1 s (reference pulses) and pulses with separations of 10 ms over a temperature sweep (Fig. 4a). At each temperature, we set the excitation amplitude to result in t_{inc} = 500 ns for the reference pulse and monitored the incubation of the second pulse. We observed a much more pronounced change in the incubation times close to the IMT (Fig. 4c and 4d). This difference in the incubation times is proportional to the slope of t_{inc} versus relaxation time (for example 78 ns/dec in Fig. 1c). Therefore, our results show a faster relaxation at higher temperatures (inset of Fig. 4c) which is an important feature of glass-like systems. We note that in our ultrafast electrical measurements, the characterization of t_{inc} was limited to ~55 °C (see Methods), and the trend of increasing the relaxation speed might not hold at the strong phase-coexistence regime[29], where the metallic phase becomes metastable. The results presented in Ref.[30] showing VO_2 relaxation by accurate resistance measurements, might be connected to this behavior: the relaxation rate is almost constant right at the beginning of the hysteresis region, and then it gets slower at the strong phase-coexistence regime.

Glass transitions are also reversible and can undergo new phase paths if they are re-excited before a complete relaxation. These are analogous features of our observations shown in Fig. 1f and Fig. 2b, respectively. It should be noted that we obtained identical memory effect under vacuum of 10^{-4} mbar, which shows that such off-stoichiometric mechanism must be purely configurational, without any exchange with the ambient. Even though more investigations may be needed to identify in-depth the microscopic details of this process, the observed effect certainly shares important features of glasses, thus can be considered as glass-like dynamics.

Potential applications in computation and data storage

The concept of electrically accessible glass-like dynamics can offer opportunities in electronics. An important aspect of the observed effect is that, at a constant amplitude, t_D is proportional to the energy required to activate IMT. Therefore, the history of a device determines the switching energy barrier (E_{bar}) in the future: the higher the number and frequency of switching events, the lower the energy barrier (Figs. 5a and 5b). One can model E_{bar} at $t = t_0$ in the transient regime after n pulses occurring at t_k ($1 \leq k \leq n$) by

$$E_{\mathrm{bar}} = E_0 - E_1 \ln\left(\sum_{k=1}^{n} \frac{T_0}{t_0 - t_k}\right), \quad (1)$$

where E_0 is the energy barrier of the device which is relaxed for $T = T_0$, and E_1 is a constant. The second term in the right hand side of the equation represents the reduced energy barrier due to the device history. Equation (1) captures the dynamic changes in the t_{inc} both for uniform (Fig. 5a) and non-uniform pulse patterns (Extended Data Table 1). This functionality can enable highly dynamic classifiers with a computation-free training, which cannot be achieved in classic approaches based on nonlinear resistive elements[31]. To show this, we can consider a neural network with one hidden layer, in which a VO_2 switch is placed between each two nodes (Fig. 5c). At time t, the network can be fully described by matrices $E^A_{\mathrm{bar}}(i,j,t)$ and $E^B_{\mathrm{bar}}(j,k,t)$ representing the reduced energy barrier of A_i-X_j and X_j-B_k switches, respectively. The product of these two matrices corresponds to the correlation between inputs and outputs, enabling an energy-based classification: for each set of inputs, the output with the minimum energy required for IMT triggering at the interconnections will be activated.

This concept provides two important features. First, training of the network can be done purely based on hardware. There is no need for calculation of weights and also no need to physically induce them, for example to manipulate the resistivity of elements[31]. We show this feature in classification of three characters "I", "J", and "L" provided in 3×3 pixels (Fig. 5d). Application of electric currents to the input nodes (A_i) corresponding to each image label, and grounding the equivalent output, can simply train the network. For example, to train the network with sample "J", the input nodes A_2, A_4, A_7, A_8, and A_9 are activated and B_2 is grounded, while all other nodes are floating. This reduces the energy barrier for some of the pathways connecting each set of inputs to the corresponding output. Fig. 5e illustrates the $E^A_{\mathrm{bar}} \times E^B_{\mathrm{bar}}$ matrix with a color map, representing the effective reduced energy barrier from inputs to outputs. For example in case of sample "J", the nodes A_2, A_4, A_7, A_8, and A_9

have a lower energy barrier to fire IMTs towards output B_2 (corresponds to "J"). In this case, if one activates the above-mentioned nodes, a higher current will be collected in node B_2. This approach yields a successful classification of the characters (Fig. 5f). The second feature provided by a glassy neural network is its self-tuning capability. The system is operational after an initial training, however, it fine tunes itself as it is exposed to the classification samples, because each sample would induce switching events at the correct nodes, reducing their energy barriers. This can self-optimize the network during the classification process, only relying on a small training set.

The concept of electrically-accessible glass-like states can also enable high-performance data storage platforms (Extended Data Fig. 10 and Extended Data Table 2). This is because the triggering process is fast, the relaxation is quite slow, and the manipulation capability enables storing multi-bits on a single physical bit. In addition, the memory effect can be accessed at very low voltages ($\ll$ 500 mV) which is beneficial for energy efficient electronics[32] (Fig. 4d). Furthermore, the concept – relying on two-terminal devices – is compatible with a cross-bar configuration which offers extremely high data-storage densities[33]. The inset of Fig. 5g shows a 50 nm × 200 nm VO_2 nano-switch, in which the device history can be *read* in sub-10 ns (Fig. 5g). The *writing* process (triggering the IMT which induces the memory) can take place in sub-nanosecond time scales with low energy cost ~100 fJ (Fig. 5h). We note that a considerable portion of the measured current in the device shown in the inset of Figs. 5g-h is from fringing current that can be eliminated by defining a mesa region around the device. Therefore, the writing energy cost can go well below 100 fJ.

We also add that the demonstration of the memory effect in four-terminal cross structures open possibilities in implementations for computational and memory devices. For neural networks, the vertical direction (Fig. 3d) can be considered as the signal propagation path and the device can be programmed through independent horizontal terminals. For memory devices, this four terminal configuration enables *reading* and *writing* process to take place from different ports.

As a conclusion, our work demonstrates glass-like dynamics in VO_2 that can be excited in sub-nanosecond time scales and monitored during several orders of magnitudes in time, from microseconds to hours. A two-terminal switch undergoes complex but fully predictable and reversible dynamics, induced by a series of excitations. From a technological point of view, our results show that the response of these dynamics to a sequence of excitations can enable new schemes for data storage and processing. Our functional devices can potentially meet some of the continuous demands in electronics such as downscaling[33], fast operation[34], and decreasing the voltage supply level[32,35]. From a physical point of view, our work revealed extremely long memories in VO_2 that can be only revealed by the incubation time. Monitoring the incubation times as a sensitive measure nano-scale lattice and electronic phases can set the stage to study out-of-equilibrium phases dynamics in other material systems[36,37].

Methods

General. All the measurements have been done under controlled ambient conditions (21.5±0.5 °C), unless otherwise stated in the manuscript.

Sputtered film deposition on high resistivity Si substrates. The sputtered polycrystalline VO_2 film was 100 nm thick and deposited on a high resistivity Si substrate. A Vanadium target (99.95% pure) was used in a plasma chamber with pressure of 0.007 mbar, Oxygen flow of 22.1 sccm and Argon flow of 12.5 sccm. The substrate temperature was at 600 °C during the deposition.

Synthesis of epitaxial VO_2 on Al_2O_3 and TiO_2 substrates. The VO_2 films were grown on the (001) TiO_2 and (0001) Al_2O_3 substrates by pulsed laser deposition (PLD). For fabricating ceramic target for growing stoichiometric VO_2 films, stoichiometric V_2O_5 (99.99%, Sigma Aldrich) powder was sintered at 600°C for 18 hours. (001) TiO_2 and (0001) Al_2O_3 substrates were loaded in to high-vacuum PLD chamber and evacuated to a base pressure of ~ 1×10^{-6} Torr. Then, the prepared V_2O_5 ceramic target was ablated by focusing KrF excimer laser (λ = 248 nm) at laser fluence of 1 J/cm^2 and laser frequency of 1 Hz. VO_2 films were grown on the (001) TiO_2 substrates at TG (substrate temperature) ~ 300°C with p_{O_2} (oxygen partial pressure) of 18 mTorr and on the (0001) Al_2O_3 substrates at T_G ~ 450°C with p_{O_2} ~ 30mTorr, respectively. After growth, both samples were cooled down to room temperature at 20 °C/min. Symmetric 2θ-ω scans was performed by using high-resolution x-ray diffractometer (D8 Discover, Bruker, λ = 0.15406 nm) at Materials Imaging & Analysis Center of POSTECH (Pohang, South Korea). And temperature-dependent sheet resistance during heating and cooling cycles was measured at a van der Pauw geometry by using Hall measurement system.

Fabrication of VO_2 switches with micron-range gap distances. After VO_2 film synthetization and dicing the samples into 1 cm x 1 cm chips, the fabrication process was followed by an electron-beam physical vapor deposition. Different metallic layers (Ti/Au, Ti/Pt, and Pt) were used, all

with 200-nm thickness. In case of using Ti as the adhesion layer, the corresponding thickness was 10 nm. The gap was defined using a lithography step with 375-nm laser (photoresist: AZ nLoF 2020), following by ion beam etching. Then the definition of pads and mesa was performed, using the same lithography and etching technique.

Fabrication of VO_2 nano-switches. For nano-device fabrication on VO_2-on-Sapphire, the process was started by a metal deposition (1 nm Cr / 40 nm Au / 1 nm Cr). Then, an electron-beam lithography step with a 50% ZEP resist (a styrene methyl acrylate-based positive e-beam resist; baked at 180 °C) followed by ion-beam etching was employed to form the nano-gaps and radiofrequency pads.

High-bandwidth large-signal measurement. High-frequency electrical measurements typically are performed in the frequency domain, where the device under test is characterized based on scattering matrix parameters. This method, however, is not able to capture large-signal switching transients. Instead, we used a time-domain measurement technique, where the device is excited by a pulse generator with 3-ns rise-time, and switching transient of the VO_2 device is measured with an ultra-high speed oscilloscope with a DPO70000SX 70-GHz Tektronix oscilloscope. To achieve an extremely precise measurement, we used radiofrequency probes with Groud-Signal-Ground (GSG) configuration, which provide 67-GHz bandwidth. The voltage waveform at the 50-Ω port of oscilloscope were measured. Dividing the measured voltage by 50-Ω results in the current flowing through the VO_2 film.

Thermal measurements. Thermal measurements were performed using a Quantum Focus Instrument (QFI) IR microscope with a 512-by-512-pixel InSb IR detector array cooled using liquid nitrogen. This setup is equipped with lenses and filters providing 20x optical magnification, high resolution (~2.8μm) and accuracy. An active thermal stage with a thermoelectric module, forced convection heat sink and a precise temperature controller, enabled an accurate emissivity correction using the factory-provided calibration data. In addition, to increase the emissivity of the chips and to avoid errors due to the IR transparency of the layers, a black paint was used on top of the chips. For all of the measurement points in this work accurate pixel-by-pixel emissivity calibrations was performed to ensure valid measurements. The transient temperature measurements were limited to the frame rate of the 26.71 frame/sec due to the processing and data transfer delays between the module and the computer.

Measurements on the VO_2 crosses. We used a transformer to isolate the vertical and horizontal excitations of the VO_2 cross (Fig. 3d). In this case, no net charge transfer is possible between terminals 1-2 and 3-4, since the horizontal and vertical signals do not share the ground. To make sure that IMT takes place in the horizontal direction, we measured the voltage signal after the transformer with a 1-GHz differential probe (which does not impose the global ground to terminals 3 and 4).

The vertical direction was terminated by the 50-Ω port of a 70-GHz scope which limited the current passing through terminals 1 and 2. To limit the current in the horizontal direction we used an off-chip 100-Ω resistor. We always supplied a 500-mV dc voltage (V_{low} in Fig. 3e) to terminal 1 and monitored the vertical current flow at terminal 4 (in Fig. 3e, the current is non-zero for $t < 0$). This is to make sure that the phase transition area due to triggering the horizontal path do not reach the vertical pads. Therefore, the observed memory effect in the vertical direction is solely due to exciting the VO_2 channel and not the metal-VO_2 junction.

High-temperature ultrafast measurements. As shown in the schematic of the experimental setup presented in Fig. 1a, the ultrafast electrical measurements were done in a two-port configuration, in which both function generator and the oscilloscope have 50-Ω terminations, which is necessary for precise high-bandwidth measurements. At the same time, these 50-Ω terminations limit the current passing though the device, especially when VO_2 is in the metallic state. This a beneficial aspect because it avoids overheating and damaging the device, which enables a degradation-free operation (Extended Data Fig. 2c).

For high-temperature measurements, the resistance of the OFF state becomes significantly lower, getting close to the resistance of the metallic phase. This results in a rather small ON/OFF ratio. In this case, even the 50-Ω series resistances dominate both ON state and OFF state resistances, and the insulator-metal switching was not detectable. Therefore the characterization of the relaxation time at the strong phase-coexistence regime (T > 55 °C, see Extended Data Fig. 2b) was not possible with our ultrafast technique.

Multi-level ultra-scaled memory. The results reported in Fig. 2 present a multi-level memory concept, in which the information is stored in nano-scale atomic/molecular configurations, as an alternative to charge-based memory devices. This can be realized by two-port switches with nano-gaps, which have the potential capability to be implemented

in a cross-bar configuration resulting in extremely high densities. Fig. 5g shows the switching transient of a 50-nm-long gap VO_2 switch, for different values of relaxation times. Nano-devices exhibit similar memory effect in much shorter incubation times, which enables a reading time below 10 ns. Fig. 5h shows that triggering IMT in a nano-device by an over-threshold pulse can be even much faster than 10 ns (well below 1 ns) with an energy consumption in range of 0.1 pJ. This enables a sub-nanosecond writing process. Extended Data Fig. 10a illustrates a potential implementation of a multi-level Mott-based memory, which includes three reference bits (R_1, R_2, and R_3) together with a row of data bits (B_k, $1 < k < n$). Each bit corresponds to a two-port VO_2 switch. For writing a row of bits, the three reference bits are respectively written with N_1, N_2, and N_3 pulses. Applying different number of pulses to each bit B_k induces four distinct states: written with N_1, N_2, N_3, or nothing. For reading, initially the first reference bit is submitted to a series of pulses with increasing widths, until the IMT is triggered (Extended Data Fig. 10b). This indicates the pulse width W_k required to trigger IMT in those bits that were written with N_k pulses. We call this the key pulse corresponding to the reference bit R_k (Extended Data Fig. 10c). Then, key pulses 1, 2, and 3 are applied to data bits (Expended Data Fig. 10d), and the first pulse that triggers IMT determines the written data. If none of the pulses trigger IMT, it has not been written. The scheme just relies on a fixed amplitude with changing the pulse-width, which is straightforward in electronics.

Validation of Eq. 1 in a non-uniform pattern. We examined the accuracy of Eq. 1 in a non-uniform patter of pulses with the following separations: 1s, 10ms, 1ms, 100ms, 1ms, 1ms, 1ms. We periodically repeated this pattern and measured the corresponding incubation times.

Eq. 1 represents the energy barrier after n switching events. The equation can be equivalently written for the incubation times:

$$t_{\mathrm{inc}} = t_{\mathrm{inc},0} - t_1 \ln\left(\sum_{k=1}^{n} \frac{T_0}{t_0 - t_{\mathrm{k}}}\right), \tag{2}$$

where $t_{\mathrm{inc},0}$ represents the incubation time of the switch relaxed for $T = T_0$ after n excitations. In this case we consider the pulse after the longest relaxation (T_0 = 1 s) as the reference pulse (with incubation time $t_{\mathrm{inc},0}$). Using (2) we write the reduced incubation time of each pulse with respect to the reference pulse:

$$t_{\mathrm{inc},0} - t_{\mathrm{inc}}^{\mathrm{pulse}\ 1} = t_1 \log\left(\tfrac{1}{0.01}\right) = 2t_1 \tag{3.1}$$

$$t_{\mathrm{inc},0} - t_{\mathrm{inc}}^{\mathrm{pulse}\ 2} = t_1 \log\left(\tfrac{1}{0.001} + \tfrac{1}{0.011}\right) = 3.038t_1 \tag{3.2}$$

$$t_{\mathrm{inc},0} - t_{\mathrm{inc}}^{\mathrm{pulse}\ 3} = t_1 \log\left(\tfrac{1}{0.1} + \tfrac{1}{0.101} + \tfrac{1}{0.111}\right) = 1.461t_1 \tag{3.3}$$

$$t_{\mathrm{inc},0} - t_{\mathrm{inc}}^{\mathrm{pulse}\ 4} = t_1 \log\left(\tfrac{1}{0.001+0.101+0.102+0.112}\right) = 3.012t_1 \tag{3.4}$$

$$t_{\mathrm{inc},0} - t_{\mathrm{inc}}^{\mathrm{pulse}\ 5} = t_1 \log\left(\tfrac{1}{0.001} + \tfrac{1}{0.002} + \tfrac{1}{0.102} + \tfrac{1}{0.103} + \tfrac{1}{0.113}\right) = 3.184t_1 \tag{3.5}$$

$$t_{\mathrm{inc},0} - t_{\mathrm{inc}}^{\mathrm{pulse}\ 6} = t_1 \log\left(\tfrac{1}{0.001} + \tfrac{1}{0.002} + \tfrac{1}{0.003} + \tfrac{1}{0.103} + \tfrac{1}{0.104} + \tfrac{1}{0.114}\right) = 3.27t_1 \tag{3.6}$$

Based on these calculations, the only parameter describing the transient change in the incubation times is t_1 which is equal to the change of incubation time by one decade change in the relaxation time. Using t_1 = 68.5 ns we have the values reported in Extended Data Table 1 which show excellent agreements with the measurement results.

Data availability statement. All the data supporting the claims of this paper are available from the corresponding authors upon reasonable request.

References

1. Dagotto, E. Complexity in strongly correlated electronic systems. *Science* **309**, 257–262 (2005).
2. Shao, Z. W., Cao, X., Luo, H. Jin, J.,P. Recent progress in the phase-transition mechanism and modulation of vanadium dioxide materials. *NPG Asia Mater.* **10**, 581−605 (2018).
3. Oh, S. *et al.* Energy-efficient Mott activation neuron for full-hardware implementation of neural networks. *Nat. Nanotechnol.* **16**, 680–687 (2021).
4. Bohaichuk, S. M. *et al.* Fast Spiking of a Mott VO_2-carbon nanotube composite device. *Nano Lett.* **19**, 6751–6755 (2019).
5. Briggs, R. M., Pryce, I. M., Atwater, H. A. Compact silicon photonic waveguide modulator based on the vanadium dioxide metal-insulator phase transition. *Opt. Express* **18**, 11192–11201 (2010).
6. Strelcov, E., Lilach, Y., Kolmakov, A. Gas sensor based on metal–insulator transition in VO_2 nanowire thermistor. *Nano Lett.* **9**, 2322–2326 (2009).
7. Eyert, V. The metal-insulator transitions of VO_2: A band theoretical approach, *Ann. Phys. (Leipzig)* **11**, 650-702 (2002).
8. del Valle, J. *et al.*, Spatiotemporal characterization of the field-induced insulator-to-metal transition. *Science* **373**, 907 (2021).
9. Nakano, M. *et al.* Collective bulk carrier delocalization driven by electrostatic surface charge accumulation, *Nature* **487**, 459–462 (2012).
10. Shukla, N. *et al.* A steep-slope transistor based on abrupt electronic phase transition. *Nat. Commun.* **6**, 1–6 (2015).
11. Liu, M. *et al.* Terahertz-field-induced insulator-to-metal transition in vanadium dioxide metamaterial, *Nature* **487**, 345–348 (2012).

12. Gao, X., Rosário, C. M. M., & Hilgenkamp, H. Multi-level operation in VO_2-based resistive switching devices. *AIP Advances* **12**, 015218 (2022).

13. del Valle, J. *et al.* Subthreshold firing in Mott nanodevices. *Nature* **569**, 388–392 (2019).

14. Fisher, B., Patlagan, L. & Reisner, G. M. Sliding twin-domains in self-heated needle-like VO_2 single crystals. *Sci. Rep.* **10**, 6833 (2020).

15. del Valle, J. *et al.* Generation of Tunable Stochastic Sequences Using the Insulator–Metal Transition. *Nano Lett.* **22**, 1251−1256 (2022).

16. Samizadeh Nikoo, M. *et al.* Nanoplasma-enabled picosecond switches for ultrafast electronics. *Nature* **579**, 534–539 (2020).

17. Shabalin, A. G., del Valle, J., Hua, N., Cherukara, M. J., Holt, M. V., Schuller, I. K. & Shpyrko, O. G., Nanoscale Imaging and control of volatile and non-volatile resistive switching in VO_2. *Small* **16**, 2005439 (2020).

18. Strukov, D. B., Snider, G. S., Stewart, D. R. & Williams, R. S. The missing memristor found. *Nature* **453**, 80–83 (2008).

19. Wei, J., Wang, Z., Chen, W. & Cobden, D. H. New aspects of the metal–insulator transition in single-domain vanadium dioxide nanobeams. *Nature Nanotech.* **4**, 420–424 (2009).

20. Ramírez, J. G., Sharoni, A., Dubi, Y., Gómez, M. E. & Schuller, I. K. First-order reversal curve measurements of the metal-insulator transition in VO2: signatures of persistent metallic domains. *Phys. Rev. B* **79**, 235110 (2009).

21. Abreu, E. et al. Nucleation and growth bottleneck in the conductivity recovery dynamics of nickelate ultrathin films. *Nano Lett.* **20**, 7422 (2020).

22. Cheng, S. *et al.* Inherent stochasticity during insulator–metal transition in VO_2. *Proc. Natl. Acad. Sci.* **118**, e2105895118 (2021).

23. Sohn, A., Kanki, T., Sakai, K., Tanaka, H. & Kim, D.-W. Fractal nature of metallic and insulating domain configurations in a VO_2 thin film revealed by Kelvin probe force microscopy. *Sci. Rep.* **5**, 10417 (2015).

24. Vaskivskyi, I. et al. Controlling the metal to insulator relaxation of the metastable hidden quantum state in 1T-TaS2. *Sci. Advances* **1**, e1500168 (2015).

25. Lee, S. *et al.* Electronic structure and insulating gap in epitaxial VO_2 polymorphs. *Appl. Mater.* **3**, 126109 (2015).

26. He, Z. & Millis, A. J. Photoinduced phase transitions in narrow-gap Mott insulators: the case of VO_2. *Phys. Rev. B* **93**, 115126 (2016).

27. Palmer, R. G., Stein, D. L., Abrahams, E. & Anderson, P. W. Models of hierarchically constrained dynamics for glassy relaxation. *Phys. Rev. Lett.* **53**, 958–961 (1984).

28. Heckshera, T., Torchinskyb, D. H., Klieberc, C., Johnsonc, J. A., Dyrea, J. C. & Nelsonc, K. A. Toward broadband mechanical spectroscopy. *Proc. Natl Acad. Sci.* 114, 8710–8715 (2017).

29. Qazilbash, M. M. *et al.* Mott transition in VO_2 revealed by infrared spectroscopy and nano-imaging. *Science* **318**, 1750–1753 (2007).

30. Claassen, J. H., Lu, J. W., West, K. G. & Wolf, S. A. Relaxation dynamics of the metal-semiconductor transition in VO_2 thin films. *Appl. Phys. Lett.* **96**, 132102 (2010).

31. Prezioso, M. *et al.* Training and operation of an integrated neuromorphic network based on metal-oxide memristors. *Nature* **521**, 61–64 (2015).

32. Ionescu, A. M. & Riel, H. Tunnel field-effect transistors as energy-efficient electronic switches. *Nature* **479**, 329–337 (2011).

33. Pi, S. *et al.* Memristor crossbar arrays with 6-nm half-pitch and 2-nm critical dimension. *Nat. Nanotechnol.* **14**, 35–39 (2019).

34. Wang, P. F. *et al.* A semi-foating gate transistor for low-voltage ultrafast memory and sensing operation. *Science* **341**, 640–643 (2013).

35. Manca, N. *et al.* Selective high-frequency mechanical actuation driven by the VO_2 electronic instability. *Adv. Mater.* **29**, 1701618 (2017).

36. Hollander, M. J. *et al.* Electrically driven reversible insulator–metal phase transition in 1T-TaS_2. *Nano Lett.* **15**, 1861–1866 (2015).

37. Grimaldi, E. *et al.* Single-shot dynamics of spin–orbit torque and spin– transfer torque switching in three-terminal magnetic tunnel junctions. *Nat. Nanotechnol.* **15**, 111–117 (2020).

38. J. J. Yang, D. B. Strukov, & D. R. Stewart, Memristive devices for computing. *Nature Nanotechnol.* **8**, 13–24 (2013).

Author contributions. M.S.N and E.M. conceived the project. M.S.N, E.M. and P.M. proposed the mechanism hypothesis. A. Krammer, Y.P., A.S., and J.S. synthesized the VO_2 films. M.S.N. fabricated the devices and performed and analyzed the electrical measurements. R.S. performed and analyzed thermal microscopy measurements. G.M.M. and A.Kis performed and analyzed KPFM measurements. M.S.N. and E.M. wrote the manuscript with input from all authors.

Acknowledgements. We are grateful to the help of the staff at the Center of Micro and Nano Technology (CMi) at EPFL with the fabrication process. We thank A. Ionescu for discussions. Y.K. and J.S. acknowledge support for PLD growth from the Basic Science Research Program (2020R1A4A1018935) through the National Research Foundation of Korea (NRF) funded by the Ministry of Science and ICT.

Competing interests. The authors declare no competing interests.

Correspondence and requests for materials should be addressed to E.M. and M.S.N.

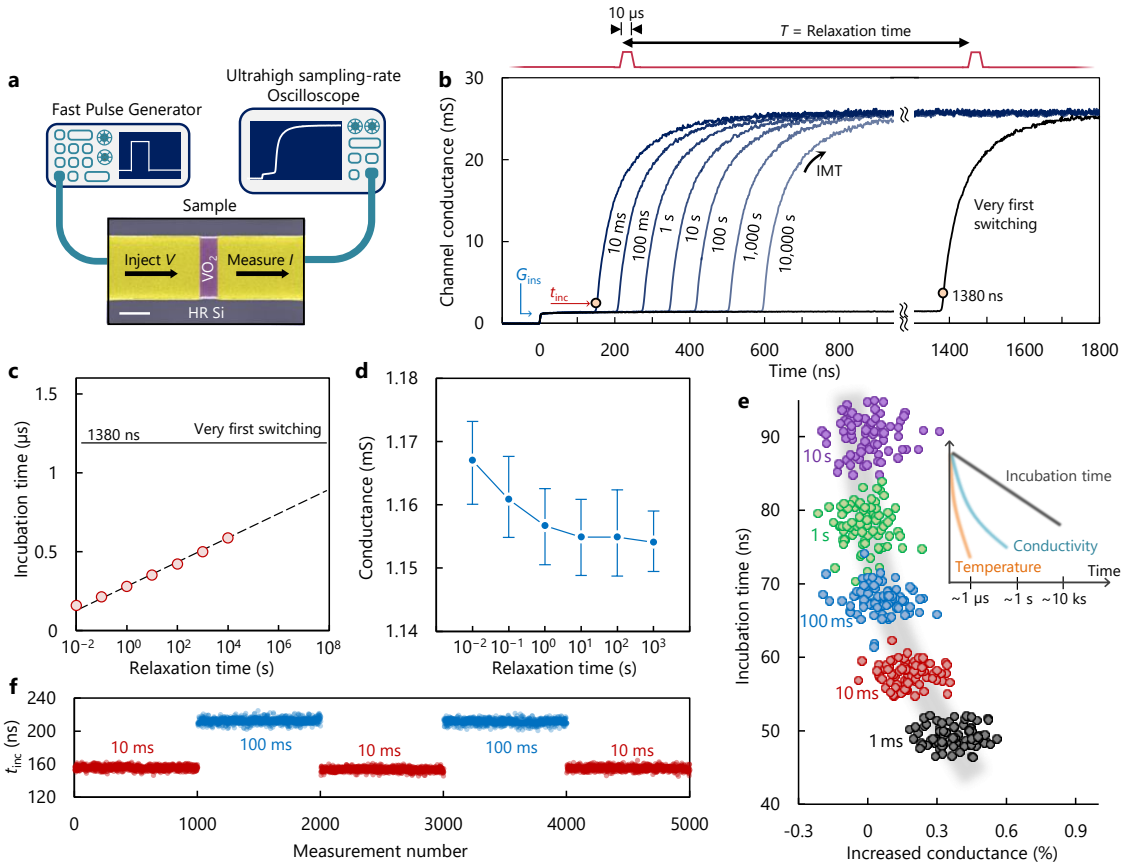

Fig. 1 | Tracing state dynamics of VO_2 switches with incubation time. a, Schematic of the ultrafast time domain experimental setup. The SEM image shows the VO_2 switch (scale bar corresponds to 5 μm). The devices investigated had lengths varying from 50 nm to 3 µm. **b,** Transient conductance of the VO_2 channel corresponding to different relaxation times T, as well as the very first switching cycle. The incubation time (t_{inc}) and the conductance of the insulating-state (G_{ins}) were studied. **c,** Incubation time versus relaxation time. t_{inc} shows a logarithmic function of T. The error bars are smaller than the point dimension. **d,** G_{ins} versus relaxation time. After ~1 s, variations in the conductance can no longer be detectable. **e,** Incubation time versus increased conductance ($(G_{ins} - \bar{G})/G_{ins}$, where $\bar{G}$ is the average over G_{ins} for measurements corresponding to 10 s relaxation) for different relaxation for a 100-nm-long device, showing the reproducibility of the results. The inset illustrate the fast relaxation of temperature and resistance, and the slow dynamics of t_{inc}. **f,** Monitored incubation time for 5,000 measurements with two different relaxation times 10 ms and 100 ms, showing that the effect is reversible and consistent.

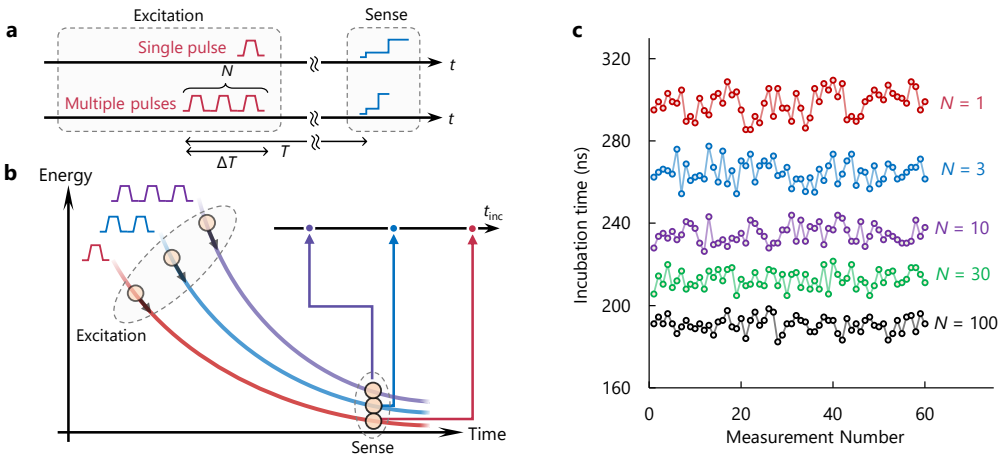

Fig. 2 | Manipulation of post-firing state of VO_2 switches. a, Schematic showing excitation of the VO_2 switch with single or multiple pulses and monitoring of the t_{inc} at the sensing pulse after a long relaxation time T. **b,** After multiple pulses, the film undergoes different relaxation trajectories, and monitoring t_{inc} can identify the different original excitations. **c,** Measured t_{inc} for different excitation pulse numbers (N) for ΔT = 1 ms and T = 1 s.

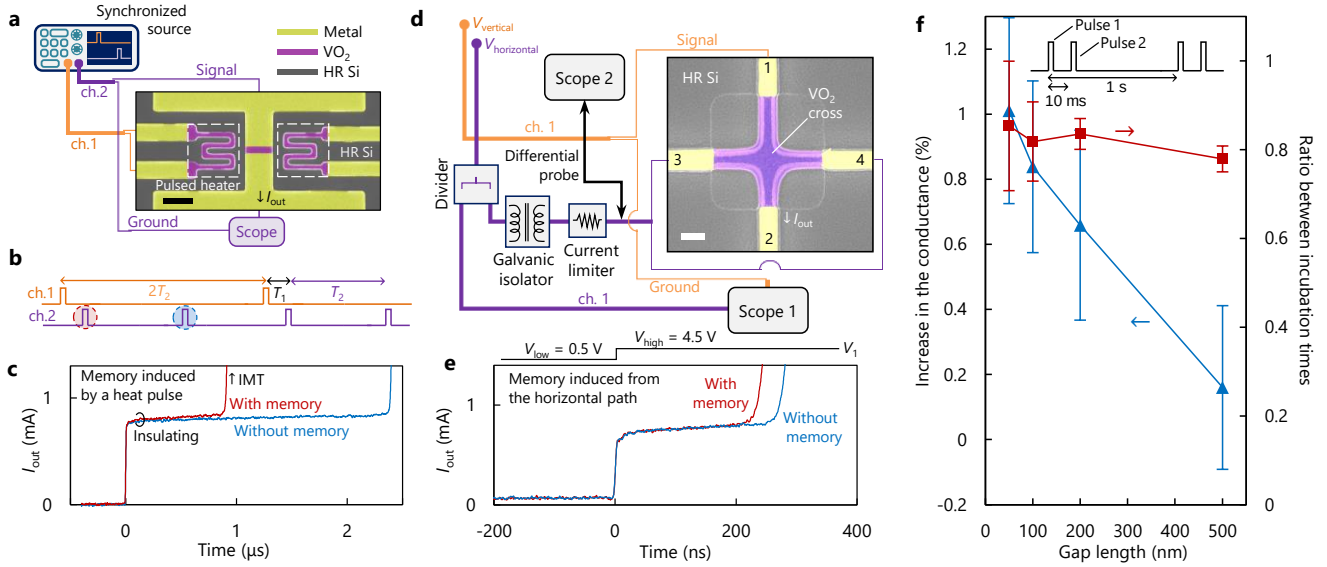

Fig. 3 | Exploration on possible mechanisms behind the long memory. a, Schematic of an experimental setup for a synchronized measurement in which the memory is induced by a heat pulse. **b,** Illustration of waveforms in the synchronized measurement. Channel 1 triggers the IMT in isolated pulsed heaters which ensures thermal-driven phase transition in the middle switch. The effect of the heat-induced IMT is evaluated in the incubation of the middle switch excited by Channel 2. **c,** Measurements indicate that the memory can be induced by thermal IMT, showing the generality of the effect. **d,** Schematic of an experimental setup for a synchronized measurement on a VO_2 cross structure. The effect of IMT triggering in the horizontal path is measured by monitoring the incubation time in the vertical path. The scale-bar of the false-colored SEM image corresponds to 2 μm. **e,** Output current at terminal 4 of the cross with a 1-s history of IMT triggered in the horizontal path (red) and without that (blue). This indicates that the memory effect originates from the VO_2 channel, and rules out the possible effect from the VO_2-metal junction. **f,** Evaluation of the memory effect on VO_2 devices with different gap lengths ranging from 50 nm to 500 nm. While devices with smaller channel lengths show a higher increase in the conductance, the memory embedded in the incubation time is nearly constant (Extended Data Fig. 8).

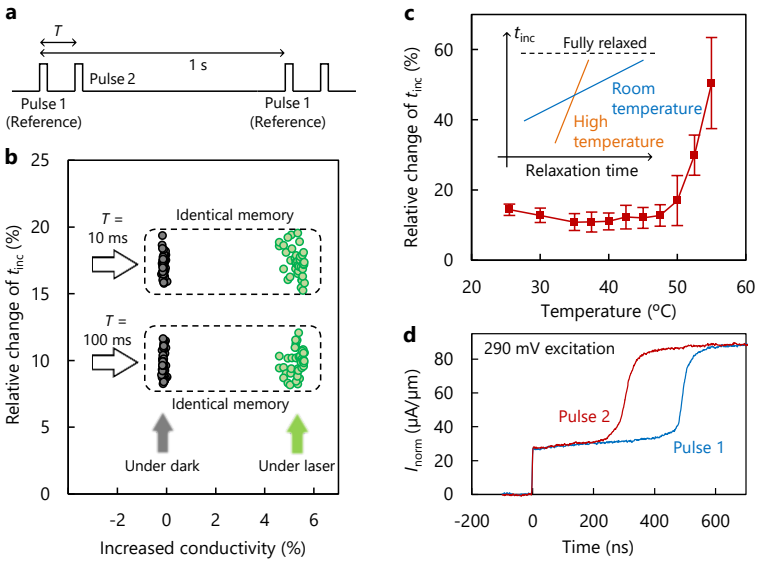

Fig. 4 | Evidence of glass-like dynamics. a, Illustration of excitation signal of a VO_2 switch for measurements under laser light. Every second, two identical pulses with the time separation T are applied to the device and incubation times are monitored ($t_{\mathrm{inc}}^{\mathrm{ref}}$ and t_{inc}, respectively). **b,** Relative change in the incubation time ($(t_{\mathrm{inc}} - t_{\mathrm{inc}}^{\mathrm{ref}})/t_{\mathrm{inc}}^{\mathrm{ref}}$) versus increased G_{ins} in a 200-nm-long channel VO_2 switch. Measurements under a continuous-wave 532-nm laser light with a power density of ~100 W cm^{-2} show a considerably higher conductivity, however, the memory effect is unchanged. The experiment shows that the memory effect is likely structural. **c,** Relative change in the incubation time after T = 10 ms with respect to reference pulses with relaxation time of T = 1 s at different temperatures. The more pronounced change in t_{inc} at high temperatures indicates a faster relaxation (inset). **d,** Transient current density of the VO_2 switch corresponding to two consecutive triggering with V_{set} = 290 mV at chuck temperature of 55 °C. The results show a notable change in t_{inc}.

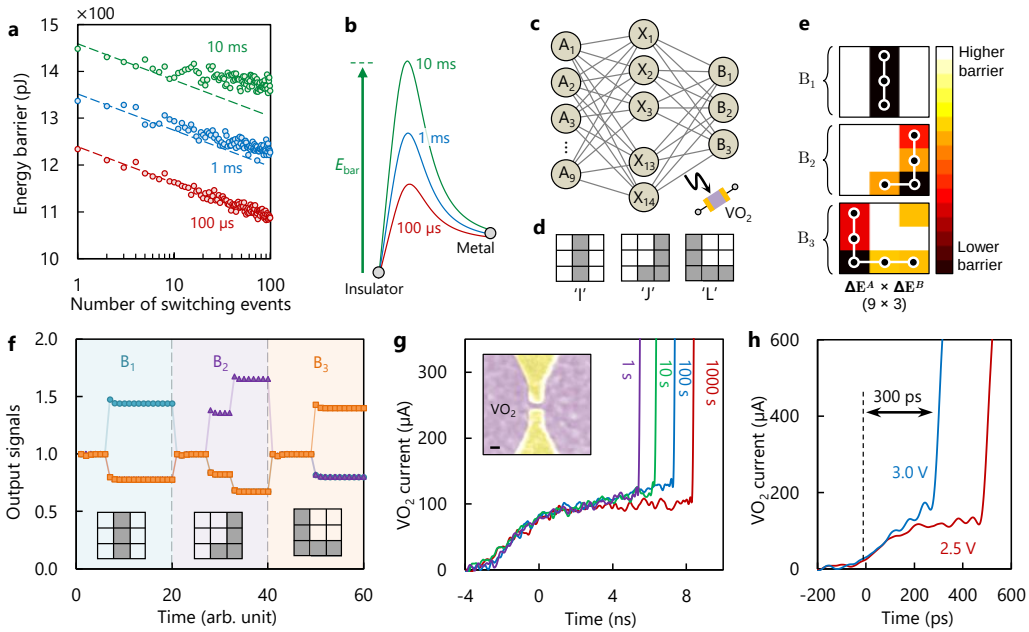

Fig. 5 | Electrical control of glass-like dynamics for computation and data storage. a, Dynamic change in energy barrier (E_{bar}) of a 2-μm-long VO_2 switch with the number of switching events for different pulse separations. **b,** Schematic showing that shorter pulse separations result in a lower E_{bar}. **c,** Considered neural network. A VO_2 switch is placed in the interconnection between each two nodes. ΔE^A and ΔE^B matrices represent the reduced energy barriers corresponding to A_i-X_j and X_j-B_k interconnections. **d,** Labels used to train a 3 × 3 pixel network for image classification. **e,** Post-training $\Delta E^A \times \Delta E^B$ matrix represents the effective reduced energy barrier corresponding to each output. **f,** Output signals at the three nodes B_1 (circles), B_2 (triangles), and B_3 (squares). Exposing the network to the inputs and monitoring the output currents successfully classifies the samples. **g,** Measured current of a VO_2 nano-device showing the potential of glass-like relaxation for ultra-scaled memory devices. The inset shows the false-colored scanning microscope image of the VO2 switch. The scale bar correspond to 100 nm. **h,** Measured current of the VO_2 nano-device (represented in the inset of part **g**) excited with V_{set} = 2.5 V (red line) and V_{set} = 3.0 V (blue line), showing that electrically induced memory can take place in sub-nanosecond time scales.

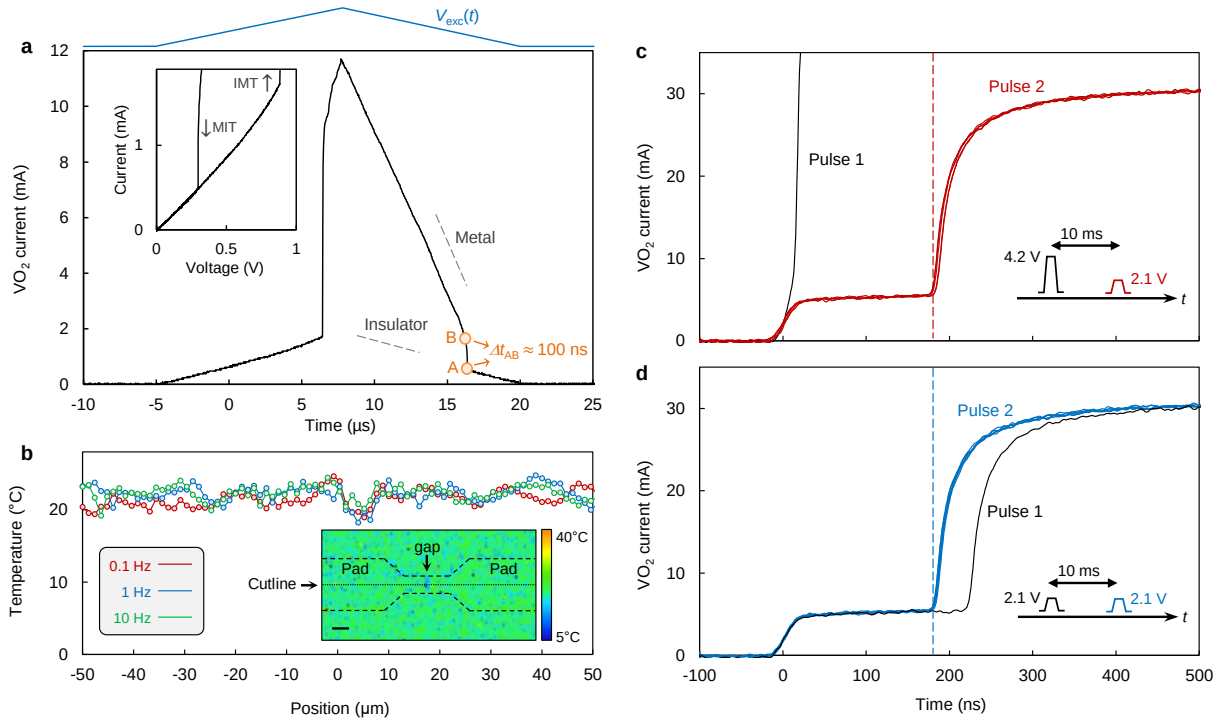

Extended Data Fig. 1 | Investigation on the possible effect of temperature rise on the observed memory effect. **a,** Measured current of a VO_2 switch under triangular excitation. The MIT transition happens between points A and B with a short time separation of $\Delta t_{AB} \approx 100$ ns. The inset presents the extracted resistance of the device in the IMT and MIT cycles showing that post excitation resistance is close (within 1%) to the pre-IMT resistance. This is another indication of the fast sub-microsecond cooling. **b,** Thermal microscopy of a two-terminal VO_2 switch triggered by 10-μs pulses (V_{set} = 2.1 V) with three different frequencies 0.1 Hz, 1 Hz, and 10 Hz. The captured average temperature over the device does not show any noticible difference between the three cases. This indicates that given the long time duration of our observed memory, this memory effect cannot be originated from thermal effects. **c, d,** Investigation of the memory effect for different excitation amplitudes V_{set} = 4.2 V and 2.1 V, respectively. If thermal effects induced the memory effect, then the 4.2 V excitation should result in a more pronounced change in the incubation time, because it leads to a higher temperature rise comparing to 2.1 V excitation. The measured incubation times, however, are identical, which disproves the role of thermal effects in our observed memory.

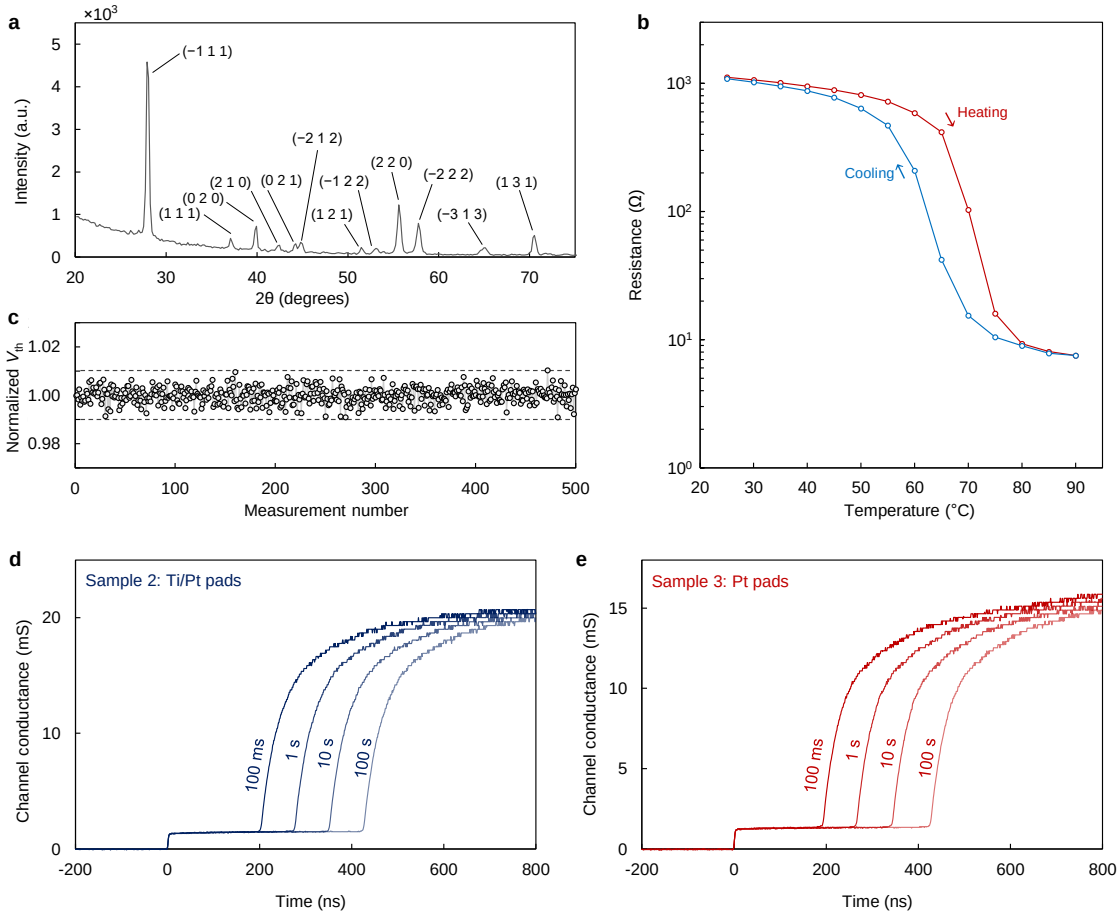

Extended Data Fig. 2 | Evaluation of Vanadium Dioxide film and fabricated devices. a, The thin film structure was determined by X-ray diffraction (XRD) analysis using an Empyrean X-ray diffractometer with monochromatic Cu Kα radiation (λ=0.154056 nm). The θ − 2θ diffraction pattern, recorded in the 20° – 75° (2θ) range. The result indicates that the sample is crystallized in the single monoclinic phase as all diffraction peaks are indexed to monoclinic VO_2 (M1) crystal structure according to PDF 04-003-4401 (Space group $P2_1/c$, a = 5.75 Å, b = 4.52 Å, c = 5.38 Å, β = 122.6°). **b,** Resistance versus temperature of a two-port VO_2 switch showing a sharp reduction at the critical temperature of VO_2. **c,** Threshold consistency indicating no degradation. A 3-µm-long VO_2 switch was excited by a voltage ramp and the threshold voltage at each IMT triggering was monitored. The results indicate less than ±1% variation with no drift, indicating no degradation in the film. **d, e,** Reproducibility of the results in devices with other metallic pads. Two-port switches fabricated on the high resistivity silicon substrate, based on VO_2 / Ti (10 nm) / Pt (200 nm) and VO_2 / Pt (200 nm) structures exhibit identical memory behavior. The results indicate that the observation is independent from metal-VO_2 interface.

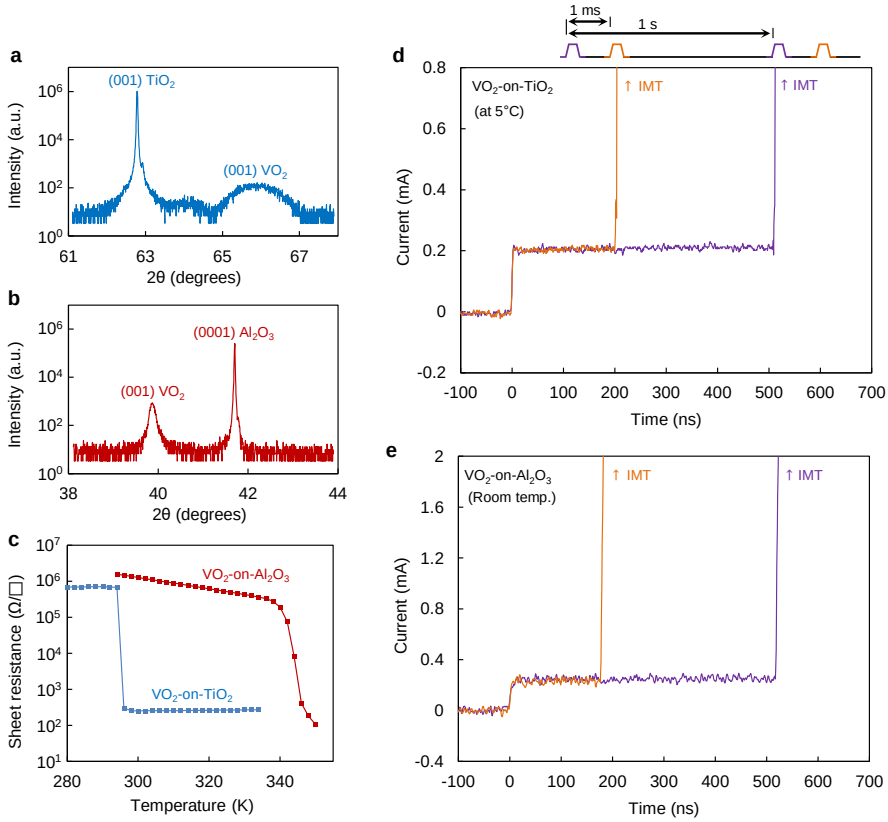

Extended Data Fig. 3 | Reproducibility of the results on a single-crystal VO_2 samples on TiO_2 and Al_2O_3 substrates. Symmetrical 2θ-θ XRD scan on the **a,** 10 nm-thick VO_2 film grown on (001) TiO_2 substrate (VO_2-on-TiO_2), and **b,** 100 nm thick VO_2 film grown on (0001) Al_2O_3 (VO_2-on-Al_2O_3). **c,** Sheet resistance measurements on VO_2-on-TiO_2 and VO_2-on-Al_2O_3 samples in the heating cycle. In case of VO_2 grown on the (001) TiO_2 substrate, which is strained along the c-axis by -1.2%, the transition temperature is shifted from ~340 K to ~292 K. **d, e,** Pulsed-measurements with two relaxation times - 1-ms and 1-s - on VO_2-on-TiO_2 and VO_2-on-Al_2O_3 samples, showing the strong dependence of t_{inc} on the relaxation time. In case of the VO_2-on-TiO_2 sample, the stage temperature was 5 °C to ensure that the film reverts back to the insulating state after removing the excitation.

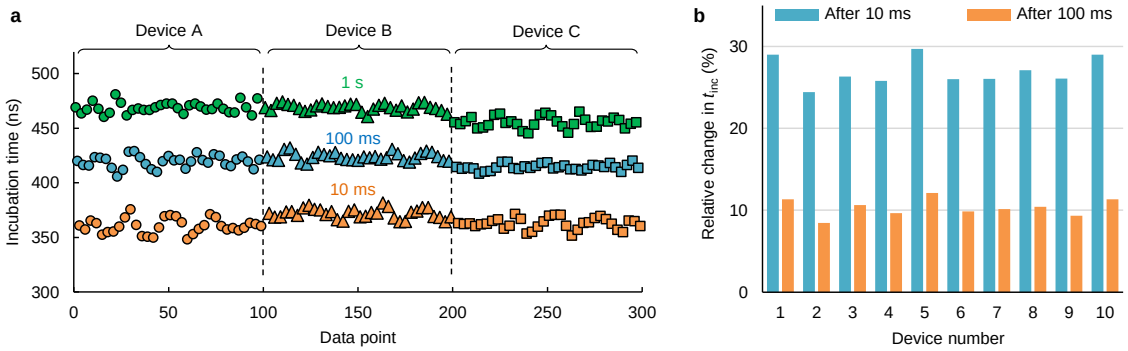

Extended Data Fig. 4 | Consistency of the observed memory effect. Applying repetitive pulses (V_{set} = 1.9 V) to a 500-nm-long channel device with periodically changing the separation times between 1s, 100 ms, and 10 ms, and monitoring the incubation time corresponding to each value of relaxation time. **a,** Measured incubation times over 100 consecutive measurements for three devices with identical geometries. **b,** Consistency of the memory effect defined as $m = t_{\mathrm{inc}}^{\mathrm{ref}}/t_{\mathrm{inc}} - 1$ for ten devices with the same geometry. $t_{\mathrm{inc}}^{\mathrm{ref}}$ is the incubation of the reference pulse (corresponding to 1 second relaxation) and t_{inc} represents the incubation time corresponding to pulses with 10 ms (blue columns) or 100 ms (orange columns) relaxation times.

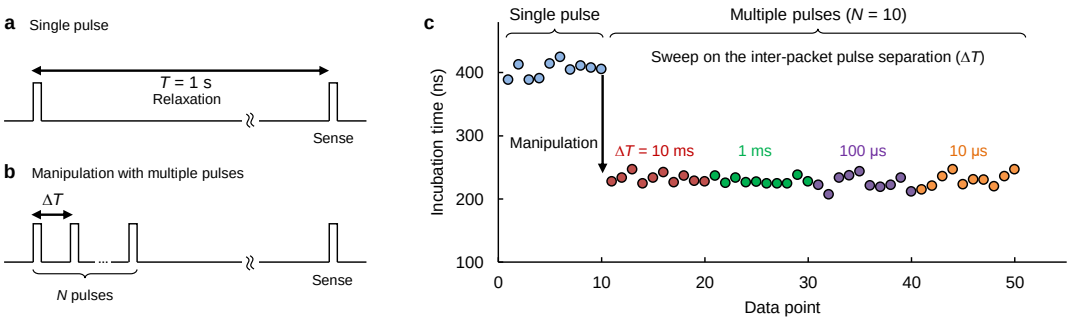

Extended Data Fig. 5 | Effect of inter-packet pulse separation on manipulation of the device state. a, Schematic of waveform corresponding to a single-pulse excitation (V_{set} = 2.7 V and 1-μs pulse width) and sensing incubation time after the relaxation time T = 1 s. **b,** Schematic of waveform corresponding to N-pulse excitation (identical pulses to part a) with inter-packet pulse separation ΔT and sensing the incubation time after the relaxation time T = 1 s. **c,** Measured incubation time on a 500-nm-long channel device for single pulse excitation and multiple pulse excitation (N = 10) with different ΔT = 10 ms, 1 ms, 100 μs, 10 μs. The results clearly shows the state manipulation capability with multiple pulse excitation, however the inter-packet pulse separation plays no role in the state manipulation.

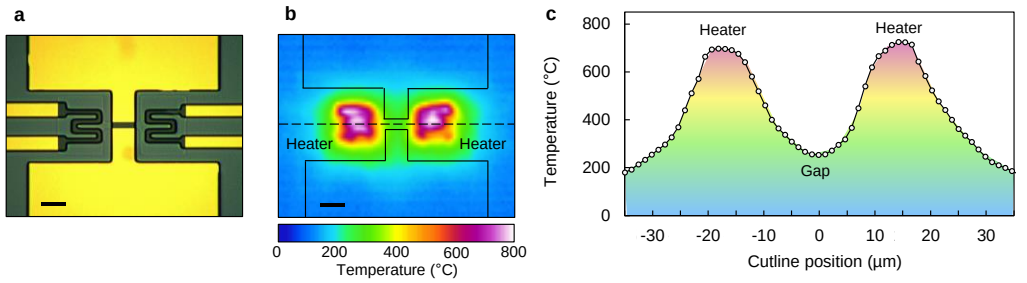

Extended Data Fig. 6 | Thermal activation of IMT using isolated heaters. a, Optical micrograph of a VO_2 switch integrated with two electrically isolated heaters. The scale bar corresponds to 10 μm. **b,** Captured thermal micrograph of the device with the heaters are triggered at their threshold voltage (18 V). The scale bar corresponds to 10 μm. **c,** Measured temperature over the cutline shown in part B indicating that the temperature at the middle switch (gap) considerably surpasses the IMT temperature. The measurement is done at the steady state, however, considering a sub-microsecond thermal time constant (Extended Data Fig. 1), for a 20-μs long excitation on the heaters, a thermal IMT in the middle switch is expected.

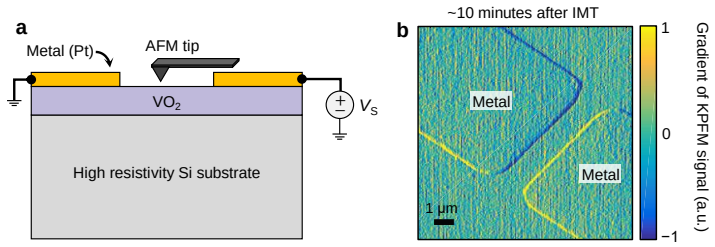

Extended Data Fig. 7 | In-situ kelvin probe force microscopy to observe possible long-lived metallic domains. a, Illustration of the KPFM experimental setup with in-situ electrical excitation to monitor possible long-lived metallic domains after electrically-driven IMT. If some metallic domains can possibly survive at room temperature and are responsible for the hours-long memory, one expects to capture a nonuniform surface potential map[38]. **b,** Gradient of the KPFM signal corresponding to the post-IMT scanning indicates visually no difference between the VO_2 layer and the metallic pads (serving as reference), which is not supportive for long-lived metallic domains at the resolution of the KPFM scan (~30 nm) to be responsible for the observed memory.

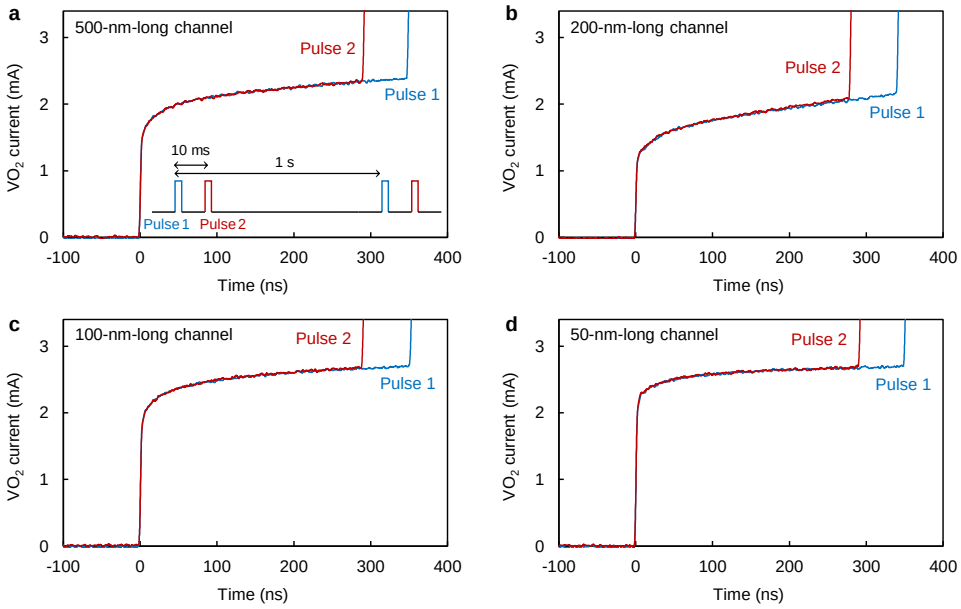

Extended Data Fig. 8 | Investigation on the effect of VO_2 channel length on the observed memory. VO_2 switches with different channel lengths ranging from 500 nm down to 50 nm and fixed width of 20 μm were investigated. The memory effect was probed by applying double pulses with relaxation times of 10 ms and 1 s. The measured VO_2 current for **a,** 500-nm-long channel VO_2 switch (V_{set} = 2.8 V). **b,** 200-nm-long channel VO_2 switch (V_{set} = 1.65 V). **c,** 100-nm-long channel VO_2 switch (V_{set} = 1.25 V). **d,** 50-nm-long channel VO_2 switch (V_{set} = 0.95 V). The voltage of each device was set to result in almost identical incubation times in the first reference pulse (blue curves). Despite the considerable difference in the VO_2 channel lengths, the second pulses exhibited similar incubation times. These results show that the memory effect is identical among devices, and not a strong function of channel length. This suggests that the observed phenomena are not attributed to any mesoscopic length scale.

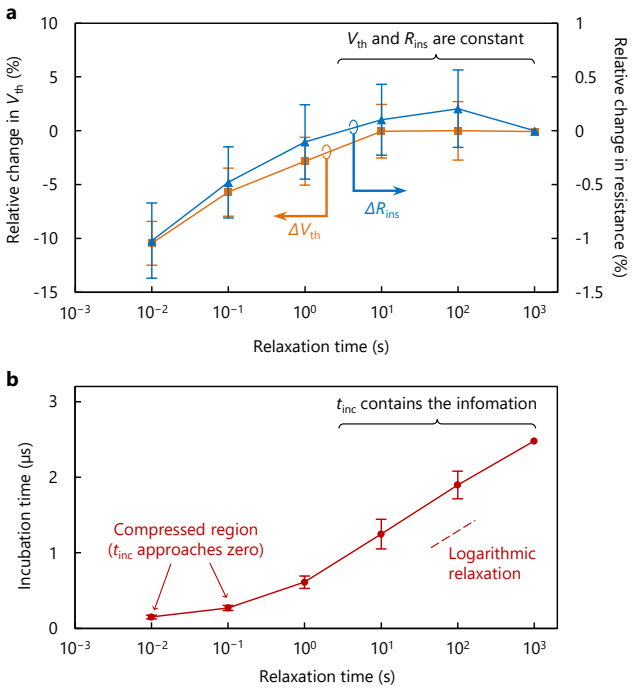

Extended Data Fig. 9 | Evaluation of threshold voltage, resistance, and the incubation time of a VO_2 switch. a, IMT threshold voltage and resistance of 1-μm-long channel VO_2 switch were measured at different relaxation times. Both parameters show similar trends, although the change in the threshold voltage is ten times larger than that of the resistance. Both parameters stabilize at in a few seconds and do not show logarithmic relaxation. We note that the MIT threshold voltage was totally independent from the relaxation time. **b,** Measured incubation revealed the information of previous switching events when the threshold and resistance are constant. Each data point corresponds to at least 20 measurements (error bars defined) with the exception of the T = 1000 s where we collected three data points. The results show that the memory effect embedded in the incubation time is independent from the changes in the threshold voltage and the resistance of the channel.

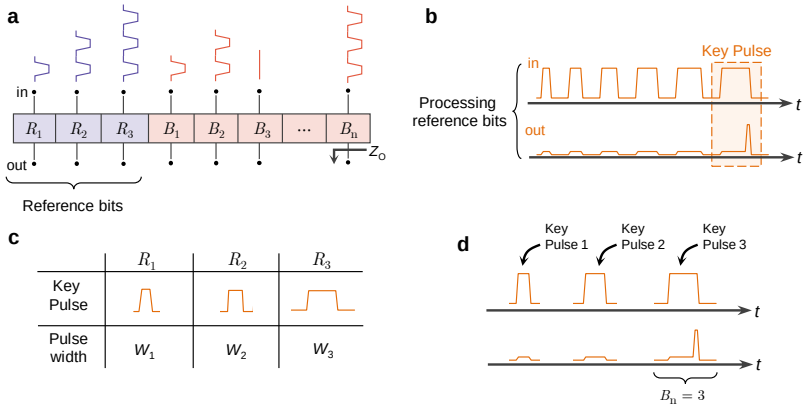

Extended Data Fig. 10 | Concept of ultrafast ultra-scaled multilevel glass-like memory in VO_2. a, Scheme of a four-level glass-like memory including three reference bits R_1, R_2, and R_3 (written by different number of pulses, N_1, N_2, and N_3, respectively) and n ordinary bit B_k. **b,** Reading process starts by processing reference bits to extract the pulse width needed to trigger IMT in each reference bit. It is possible to apply a train of pulses with increasing widths until an IMT event takes place: this gives the incubation time corresponding to a VO_2 switch which is excited by N_k pulses. It is also possible to apply a longer pulse and measure the IMT time delay (incubation time). A pulse with the width equal to the incubation time is able to fire IMT with those bits that are activated with the same number of pulses as the reference bit (N_k). We call this a key pulse. **c,** Three key pulses with pulse-widths W_1, W_2, and W_3 are obtained ($W_1 < W_2 < W_3$). **d,** Three key pulses are applied to each bit B_k to accomplish the reading process.

Extended Data Table 1 | Verification of the empirical model presented in Eq. 1 in a non-uniform pattern*

Pulse no.	Relaxation time (ms)	Measured t_{inc} (ns)	Reduction in the incubation time with respect to the reference pulse		
			Measurement (ns)	Analytical model (ns)	Error (%)
0 (Reference)	1000	778.4	-	-	-
1	10	639.1	139.3	137.0	1.7%
2	1	571.2	207.2	208.1	0.4%
3	100	680.1	98.3	100.1	1.8%
4	1	572.7	205.7	206.3	0.3%
5	1	559.9	218.5	218.2	0.2%
6	1	552.5	225.9	224.0	0.9%

*Calculations were presented in the Methods section.

Extended Data Table 2 | Comparison between the structural state-based memory and other technologies

Parameter	Glass-like memory	Memristor	SRAM	DRAM	Flash	Disk
Density (F^2)	< 4	4	120 – 200	6 – 12	4 – 6	2/3
Operating voltage (V)	290 mV*	Nonmetric bipolar, ~2	3.3 – 5	3.3	3.3 – 5	5 – 12
Energy / bit (pJ)	≲ 0.1	0.1 – 3	~0.1	2	10000	>10,000,000
Read time (ns)	~10	10 – 100	10 – 30	10 – 50	25,000	~10,000,000
Write time (ns)	~1	~10	13 – 95	10 – 50	200,000	~10,000,000
Retention time	> 2 hr	100 s to years	Power sup.	4 – 64 ms	Years	Years

* Record for elevated temperatures. The concept is operational for voltages below 1 V at room temperature.